

See discussions, stats, and author profiles for this publication at: <https://www.researchgate.net/publication/231274059>

Influence of Boundary Conditions on Sub-Millimeter Combustion

ARTICLE *in* ENERGY & FUELS · JULY 2009

Impact Factor: 2.79 · DOI: 10.1021/ef900040q

CITATIONS

5

READS

34

5 AUTHORS, INCLUDING:



Shaurya Prakash
The Ohio State University
52 PUBLICATIONS 412 CITATIONS

[SEE PROFILE](#)



R. R. Akberov
Kazan National Research Technological Un...
9 PUBLICATIONS 17 CITATIONS

[SEE PROFILE](#)



Damena Agonafer
Stanford University
16 PUBLICATIONS 41 CITATIONS

[SEE PROFILE](#)

Influence of Boundary Conditions on Sub-Millimeter Combustion

Shaurya Prakash,^{*,†,§} Roald Akberov,[†] Damena Agonafer,[‡] Adrian D. Armijo,[‡] and Mark A. Shannon[‡]

Department of Mechanical and Aerospace Engineering, Rutgers, The State University of New Jersey, Piscataway, New Jersey 08854, USA and Department of Mechanical Science and Engineering, University of Illinois at Urbana-Champaign, Urbana, Illinois 61801, USA

Received January 16, 2009. Revised Manuscript Received May 4, 2009

Growing interest in small-scale, portable energy systems such as fuel cells has necessitated the development of small-scale fuel processing or reforming systems. Many fuel reforming systems require reliable heat sources as in some cases temperatures in excess of 600°C maybe required. Sub-millimeter combustors can provide such a heat source; however, a broader set of design rules are needed for constructing systematically engineered heat sources. In this article, experimental observations and computational fluid dynamics modeling results are presented for stable and steady confined flame structures within an alumina sub-millimeter combustor. Influence of inlet flow and thermal boundary conditions are evaluated through a parametric study. The inlet flow rates and relative gas composition, the thermal boundary conditions that include thermal conductivity of the walls, convection of heat to and from the walls, and radiation of heat energy through the walls all determine the position, structure, and temperature of the reacting fluid and combustor walls. The model shows the importance of radiative heat transfer in the formation of the steady-state flame structures within the microcombustor.

Introduction

Rapid growth in the use of miniature systems for a variety of applications has prompted the development of small-scale, portable, and highly durable power sources to attempt to supply both high power and energy densities. The primary power source in most miniature or microscale systems are batteries but there has also been extensive development of microfuel cells^{1,2} as a possible alternative to batteries. Combustion-based power systems combined with opportunities for integration with fuel cells, photovoltaic systems, and other thermal energy conversion systems present another attractive alternative due to even higher energy densities of combusting hydrocarbon fuels over that of direct fuel cells and batteries.^{3–7} Toward the goal of developing small-scale and portable fuel cells, there has also been significant interest in developing fuel reformers^{8–10} for generation of clean, high purity fuel (e.g., H₂) for these energy-generation devices. Most

fuel reformers require high temperatures (~900 °C for some systems) making combustion-based systems very attractive heat sources.^{11,12} In addition, development of microscale combustion-based heat sources provides an avenue to supply high-quality heat for high-temperature microchemical reactors, engines, thrusters, and heaters.^{13–22} This article describes the influence of thermal and flow boundary conditions on flames within sub-millimeter combustors with the goal of providing data toward

* To whom correspondence should be addressed. E-mail: sprakas1@rutgers.edu. Telephone: 732-445-3797. Fax: 732-445-3124.

[†] The State University of New Jersey.

[‡] University of Illinois at Urbana-Champaign.

[§] Current address: Department of Mechanical Engineering, The Ohio State University, Columbus, OH.

(1) Chu, K. L.; Shannon, M. A.; Masel, R. I. Porous silicon fuel cells for micropower generation. *Journal of Micromechanics and Microengineering* **2007**, 17 (9), S243–S249.

(2) Yeom, J.; Mozsgai, G. Z.; Flachsbar, B. R.; Choban, E. R.; Asthana, A.; Shannon, M. A.; Kenis, P. J. A. Microfabrication and characterization of a silicon-based millimeter scale, PEM fuel cell operating with hydrogen, methanol, or formic acid. *Sens. Actuators, B* **2005**, 107 (2), 882–891.

(3) Fernandez-Pello, C. Micro-power generation using combustion: Issues and approaches. *Proceedings of the Combustion Institute* **2002**, 29, 883–899.

(4) Kyritsis, D. C.; Roychoudhury, S. C.; McEnally, E. S.; Pfefferle, L. D.; Gomez, A. Mesoscale combustion: A first step towards liquid fueled batteries. In *Experimental Thermal and Fluid Science* **2004**, 28, 7, 763–770.

(5) Schaevitz, S. B.; Franz, A. J.; Jensen, K. F.; Schmidt, M. A. In *A combustion-based MEMS thermoelectric power generator*, The 11th International Conference on Solid-State Sensors and Actuators, Munich, Germany, 2001; pp 30–33.

(6) Shannon, M. A.; Moore, G. V.; Ganley, J.; Miesse, C.; Rice, C.; Seebauer, E. G.; Masel, R. I. In *High-temperature microcombustion-based ammonia microchemical hydrogen generator reactors for PEM fuel cells*, Technical Digest Solid-State Sensors and Actuators Workshop, Hilton Head Island, SC, June 3–7, 2002; Foundation, T. R., Ed.; 2002; pp 27–30.

(7) Yang, W. M.; Chou, S. K.; Shu, C.; Li, Z. W. A prototype microthermophotovoltaic power generator. *Appl. Phys. Lett.* **2004**, 84, 3864–3866.

(8) Kim, T.; Kwon, S. MEMS fuel cell system integrated with a methanol reformer for a portable power source. *Sens. Actuators, A* **2008**, In Press.

(9) Matsuoka, K.; Shimbori, T.; Kuramoto, K.; Hatano, H.; Suzuki, Y. Steam reforming of woody biomass in a fluidized bed of iron oxide-impregnated porous alumina. *Energy Fuels* **2006**, 20 (6), 2727–2731.

(10) Muradov, N.; Smith, F. Thermocatalytic conversion of landfill gas and biogas to alternative transportation fuels. *Energy Fuels* **2008**, 22 (3), 2053–2060.

(11) Ganley, J. C.; Seebauer, E. G.; Masel, R. I. Development of a microreactor for the production of hydrogen from ammonia. *J. Power Sources* **2004**, 137 (1), 53–61.

(12) Christian; Mitchell, M.; Kenis, P. J. A. Ceramic microreactors for on-site hydrogen production from high temperature steam reforming of propane. *Lab Chip* **2006**, 6, 1328–1337.

(13) Aichlmayr, H. T. Design considerations, modeling, and analysis of micro-homogeneous charge compression ignition combustion free-piston engines, Ph.D. Thesis, University of Minnesota, 2002.

(14) Dunn-Rankin, D.; Leal, E. M.; Walther, D. C. Personal power systems. *Prog. Energy Combust. Sci.* **2005**, 31, 422–465.

(15) Ganley, J. C.; Seebauer, E. G.; Masel, R. I. Porous anodic alumina microreactors for production of hydrogen from ammonia. *AIChE J.* **2004**, 50 (4), 829–834.

(16) Lee, C.; Liamini, M.; Fréchette, L. G. In *Design, fabrication, and characterization of a microturbopump for a Rankine cycle micropower generator*, Solid-State Sensors and Actuators Workshop, Hilton Head Island, SC, 2006; pp 276–279.

better engineering of microcombustors for the variety of energy and power applications mentioned above.

In the past, studies have shown the difficulties in sustaining homogeneous combustion using premixed flames in confined spaces with a large surface-area-to-volume ratio ($>10^3 \text{ m}^{-1}$).^{23–25} To overcome some of the difficulties due to structural failure, non-premixed or catalytic combustion has been used with laminar flows and minimal influence of turbulent mixing as Reynold's numbers are often below 100.^{23,26–30} In addition, the critical role played by surfaces in reducing or preventing quenching of essential radicals has also been discussed.^{23,31,32} Other studies have evaluated the role of heat transfer,^{33–39}

-
- (17) Mehra, A.; Zhang, X.; Ayon, A. A.; Waitz, I. A.; Schmidt, M. A.; Spadaccini, C. M. A six-wafer combustion system for a silicon micro-gas turbine engine. *Journal of Microelectromechanical Systems* **2000**, *9* (4), 517–527.
- (18) Fu, K.; Knobloch, A. J.; Cooley, B. A.; Walther, D. C.; Fernandez-Pello, A. C.; Liepmann, D.; Miyasaka, K. In *Microscale combustion research for applications to MEMS rotary IC engine*, Proceedings of the 35th ASME National Heat Transfer Conference, 2001; Paper no. NHTC2001–20089.
- (19) Wu, M.-H.; Burke, M. P.; Son, S. F.; Yetter, R. A. Flame acceleration and the transition to detonation of stoichiometric ethylene/oxygen in mesoscale tubes. *Proceedings of the Combustion Institute* **2007**, *31*, 2429–2436.
- (20) Wu, M.-H.; Wang, Y.; Yang, V.; Yetter, R. A. Combustion in meso-scale vortex chambers. *Proceedings of the Combustion Institute* **2007**, *31*, 3235–3242.
- (21) Wu, M.-H.; Yetter, R. A. Development and analysis of a LTCC micro stagnation-point flow combustor. *Journal of Micromechanics and Microengineering* **2008**, *18* (12), 125016–1–125016–9.
- (22) Wu, M.-H.; Yetter, R. A. A novel electrolytic ignition monopropellant microthruster based on low temperature co-fired ceramic tape technology. *Lab Chip* **2009**, *9* (7), 910–916.
- (23) Miesse, C. M.; Masel, R. I.; Jensen, C. D.; Shannon, M. A.; Short, M. Submillimeter-scale combustion. *AIChE J.* **2004**, *50* (12), 3206–3214.
- (24) Moore, G. Failure of a thin-film mullite synthesis due to carbothermal reduction by the SiC. M.S. Thesis, University of Illinois, Urbana, 2000.
- (25) Miller, F. J.; Dietrich, D. L.; Struk, P.; Tien, J. S.; Mellish, B. P. *Premixed flames stabilized on or spreading inside microtubes*, Proceedings of the Fourth Joint Meeting of the U.S. Sections of the Combustion Institute, 2005.
- (26) Kyritsis, D. C.; Coriton, B.; Faure, F.; Rouchoudhury, S.; Gomez, A. Optimization of a catalytic combustor using electrosprayed liquid hydrocarbons for mesoscale power generation. *Combust. Flame* **2004**, *139* (1–2), 77–89.
- (27) Miesse, C. M.; Masel, R. I.; Short, M.; Shannon, M. A. Diffusion flame instabilities in a 0.75 mm non-premixed microburner. *Proceedings of the Combustion Institute* **2005**, *30*, 2499–2507.
- (28) Miesse, C. M.; Masel, R. I.; Short, M.; Shannon, M. A. Experimental observations of methane-oxygen diffusion flame structure in a sub-millimetre microburner. *Combustion Theory and Modelling* **2005**, *9* (1), 77–92.
- (29) Norton, D. G.; Vlachos, D. G. Hydrogen assisted self-ignition of propane/air mixtures in catalytic microburners. *Proceedings of the Combustion Institute* **2005**, *30*, 2473–2480.
- (30) Prakash, S.; Armijo, A. D.; Masel, R. I.; Shannon, M. A. Flame dynamics and structure within sub-Millimeter combustors. *AIChE J.* **2007**, *53* (6), 1568–1577.
- (31) Jensen, C. D. The dependence of flame/wall interactions on the composition of the walls for determining the material composition of a micro-combustor. M.S. Thesis, University of Illinois, Urbana, 2000.
- (32) Prakash, S.; Glumac, N. G.; Shankar, N.; Shannon, M. A. OH concentration profiles over alumina, quartz, and platinum surfaces using laser-induced fluorescence spectroscopy in low-pressure hydrogen/oxygen flames. *Combust. Sci. Technol.* **2005**, *177* (4), 793–817.
- (33) Ahn, J.; Eastwood, C.; Sitzki, L.; Ronney, P. D. Gas-phase and catalytic combustion in heat-recirculating burners. *Proceedings of the Combustion Institute* **2005**, *30* (2), 2463–2472.
- (34) Chen, M.; Buckmaster, J. Modelling of combustion and heat transfer in 'Swiss roll' micro-scale combustors. *Combustion Theory and Modelling* **2004**, *8* (4), 701–720.
- (35) Daou, J.; Matalon, M. Influence of conductive heat-losses on the propagation of premixed flames in channels. *Combust. Flame* **2002**, *128* (4), 321–339.
- (36) Daou, R.; Daou, J.; Dold, J. Effect of heat-loss on flame-edges in a premixed counterflow. *Combustion Theory and Modelling* **2003**, *7* (2), 221–242.
- (37) Daou, R.; Daou, J.; Dold, J. The effect of heat loss on flame edges in a non-premixed counterflow within a thermo-diffusive model. *Combustion Theory and Modelling* **2004**, *8* (4), 683–699.
- (38) Lee, D. H.; Kwon, S. Heat transfer and quenching analysis of combustion in a micro combustion vessel. *Journal of Micromechanics and Microengineering* **2002**, *12* (5), 670–676.
- (39) Ronney, P. D. Analysis of non-adiabatic heat-recirculating combustors. *Combust. Flame* **2003**, *135* (4), 421–439.
- (40) Kukuck, S.; Matalon, M. The onset of oscillations in diffusion flames. *Combustion Theory and Modelling* **2001**, *5* (2), 217–240.
- (41) Richecoeur, F.; Kyritsis, D. C. Experimental study of flame stabilization in low Reynolds and Dean number flows in curved mesoscale ducts. *Proceedings of the Combustion Institute* **2005**, *30*, 2419–2427.
- (42) Thatcher, R. W.; Omon-Arancibia, A. A.; Dold, J. W. Oscillatory flame edge propagation, isolated flame tubes and stability in a non-premixed counterflow. *Combustion Theory and Modelling* **2002**, *6*, 487–502.
- (43) Smithells, A.; Ingle, H. The structure and chemistry of flames. *J. Chem. Soc.* **1892**, *61*, 204.
- (44) McCoy, R. B.; Najm, H. N.; Ray, J. Shear layer effect on edge flame structure in a non-premixed methane-air flame. *Proceedings of the Third Joint Meeting of the U.S. Sections of the Combustion Institute*, 2003.
- (45) Cha, M. S.; Ronney, P. D. Propagation rates of nonpremixed edge flames. *Combust. Flame* **2006**, *146* (1–2), 312–328.
- (46) Crow, S. C.; Champagne, F. H. Orderly structure in jet turbulence. *J. Fluid Mech.* **1971**, *48* (3), 547–591.
- (47) Kim, N. I.; Seo, J. I.; Guahk, Y. T.; Shin, H. D. The propagation of tribrachial flames in a confined channel. *Combust. Flame* **2006**, *146*, 168–179.
- (48) Kurdyumov, V. N.; Matalon, M. Dynamics of an edge flame in a mixing layer. *Combust. Flame* **2004**, *139* (4), 329–339.
- (49) Prakash, S.; Armijo, A. D.; Masel, R. I.; Shannon, M. A. In *Characterizing non-premixed sub-millimeter combustion*, The Sixth International Workshop on Micro and Nanotechnology for Power Generation and Energy Conversion Applications, Berkeley, CA, November 29–December 1, 2006; Pisano, A. P.; Frechette, L. G., Eds.; Berkeley, CA, 2006; pp 17–20.
- (50) Prakash, S.; Armijo, A. D.; Masel, R. I.; Shannon, M. A. Flame dynamics in sub-millimeter combustors. *International Journal of Alternative Propulsion* **2007**, *1* (2/3), 325–338.
- (51) Prakash, S.; Miesse, C. M.; Masel, R. I.; Shannon, M. A., Flame structure variations in sub-millimeter combustors due to heat transfer through combustor walls. *Proceedings of the Fourth Joint Meeting of the U.S. Sections of the Combustion Institute*, 2005.
- (52) Thatcher, R. W.; Dold, J. W. Edges of flames that do not exist: flame-edge dynamics in a non-premixed counterflow. *Combustion Theory and Modelling* **2000**, *4*, 435–457.
- (53) Kessler, D. A.; Short, M. Ignition and transient dynamics of sub-limit premixed flames in microchannels. *Combustion Theory and Modelling* **2008**, *12* (5), 809–829.
- (54) Davy, H. Farther experiments on the combustion of explosive mixtures confined by wire-gauze, with some observations on flame. *Philosophical Transactions of the Royal Society of London* **1816**, *106*, 115–119.
- (55) Davy, H. Some researches on flame. *Philosophical Transactions of the Royal Society of London* **1817**, *107*, 45–76.
- (56) Rayleigh, J. W. S. The explanation of certain acoustical phenomena. *Nature* **1878**, *18*, 319–321.
- (57) Tyndal, J. *Sound*; D. Appleton & Company: New York, 1897.

Al_2O_3 combustors. The purpose of this paper is to evaluate the influence of specific flow and thermal boundary conditions, as described later, on the steady-state flame structure observed in sub-millimeter combustion through experimental observations and computational fluid dynamics (CFD) modeling. It is hoped that by relating experimental observations to existing theoretical models and identifying boundary conditions that directly influence microcombustion, this article will provide a first step to future researchers toward developing better and more efficient microcombustors.

Experimental Section

The materials, surface preparation, and fabrication procedures for the Al_2O_3 non-premixed sub-millimeter or microcombustors have been described in detail previously.^{23,27,28,30,49,50} Briefly, two alumina sheets were machined with a diamond-coated saw to yield a Y-shaped microcombustor with a nominal width of 10 mm and length of 35 mm. The combustion occurs within a 5 mm wide by 0.75 mm deep channel. The overall thickness of the alumina wall is 1 mm. External wall temperatures are recorded by using type R thermocouples (TCs, Omega Engineering Inc., Stamford, CT). Combustion gases are high-purity methane (CH_4) and oxygen (O_2), which are controlled by M100B MKS mass flow controllers and flow through attached hoses. The entire assembly is packed in between two approximately 1 in. thick insulation layers of fibrous alumina. For certain experiments, as described later, a slot is cut out in the microcombustor to install a sapphire window to permit flame structure imaging. To evaluate the effect of changing combustor wall thermal conductivity, a metal plate (Mo coated with Pt) is secured to the external wall over the reaction channel for a few experiments. The metal plate is attached using a high-temperature alumina adhesive. The exhaust and unburned gases flow freely into the ambient air. The steady-state flame structure is visualized by still-frame imaging. The still frames are captured by a Canon EOS Mark II digital camera with an attached infrared filter.

Computational Model

A 3D computational fluid dynamics (CFD) model was developed to study the role of inlet flow conditions and thermal boundary conditions on the steady-state flame structure and provide a framework for validating the observed experimental trends. The numerical investigation is done in *Fluent* version 6.2,⁵⁹ with the governing equations given in the user's guide. The model solves coupled species, momentum, diffusion, and energy equations. All thermo-physical properties except the thermal conductivity of the walls are taken to be temperature dependent.⁵⁹ All physical constants and thermochemical data are obtained from the *Fluent* database, which relies on a NIST database for source information.⁵⁹ The main assumptions used for the model are: (i) The flow remains laminar during the entire combustion process, as this has been established through previous experimental studies;²⁸ (ii) the gas-phase chemistry is infinitely fast and controlled by the rate of mixing of CH_4 with O_2 ; (iii) single-step reactions occur with rate constants following Arrhenius type dependence;⁵⁹ and (iv) surface reactions do not affect the steady-state flame structure, as the combustor is made from alumina and it has been shown that the surfaces are relatively inert and many surface reactions can be neglected to the first order.³² In addition, because of a lack of accurate models and thermochemical data for specific surface reactions on traditionally inert surfaces, no detailed predictions can be made. These assumptions have been chosen carefully to simplify the modeling efforts as the primary purpose of the model presented here is to complement and validate the trends observed in the experimental results and not to establish a theoretical foundation for the observed flame structure. To

(58) Chandrasekharan, R.; Prakash, S.; Shannon, M. A.; Masel, R. I. Change in radiative optical properties of Ta_2O_5 thin films due to high-temperature heat treatment. *Journal of Heat Transfer* 2007, 129, 27–36.

(59) *Fluent*, Fluent 6.2 User's Guide; Fluent, Inc.: Lebanon, NH, 2005.

accurately model effects of the combustion process and to describe all of the observations, detailed surface reactions would need to be included to capture second-order and higher effects, which is beyond the scope of this article.

The governing equations used for the model are described next. The description for each of the terms can be found in the nomenclature list. Eqs 1 and 2 are the conservation of species and energy respectively, such that

$$\frac{\partial}{\partial t}(\rho Y_i) + \vec{\nabla}(\rho \vec{v} Y_i) = -\vec{\nabla} \vec{J}_i + R_i \quad (1)$$

$$\frac{\partial}{\partial t}(\rho h) + \frac{\partial}{\partial x_i}(\rho u_i h) = \frac{\partial}{\partial x_i}\left(\kappa \frac{\partial T}{\partial x_i}\right) - \frac{\partial}{\partial x_i} \sum_j h_j J_j + S_h \quad (2)$$

The specific heat at constant pressure is taken as a piece-wise-polynomial function of temperature as determined in the *Fluent* database. Transport of species is modeled using multicomponent diffusion based on the Stefan–Maxwell equations to obtain the generalized Fick's law of diffusion and is given by

$$\vec{J}_i = - \sum_{j=1}^{N-1} \rho D_{ij} \nabla Y_j - D_{T,i} \frac{\nabla T}{T} \quad (3)$$

where D_{ij} is computed through the use of the Chapman–Enskog formula (eq 4) derived from the kinetic theory, such that

$$D_{ij} = 0.0188 \frac{\left[T^3 \left(\frac{1}{M_{w,i}} + \frac{1}{M_{w,j}} \right) \right]^{1/2}}{p_{\text{abs}} \sigma_{ij}^2 \Omega_D} \quad (4)$$

and where $D_{T,i}$ is a function of chemical composition and temperature and is expressed by the empirical relation

$$D_{T,i} = -2.59 \times 10^{-7} T^{0.659} \left[\frac{\sum_{i=1}^N M_{w,i}^{0.511} X_i}{\sum_{i=1}^N M_{w,i}^{0.511} X_i} - Y_i \right] \left[\frac{\sum_{i=1}^N M_{w,i}^{0.511} X_i}{\sum_{i=1}^N M_{w,i}^{0.489} X_i} \right] \quad (5)$$

The velocity field is determined by using the continuity and momentum equations, given by

$$\frac{\partial \rho}{\partial t} + \frac{\partial}{\partial x_i}(\rho u_i) = 0 \quad (6)$$

and

$$\frac{\partial}{\partial t}(\rho u_i) + \frac{\partial}{\partial x_j}(\rho u_i u_j) = -\frac{\partial p}{\partial x_i} + \frac{\partial}{\partial x_j} \left[\mu \left(\frac{\partial u_i}{\partial x_j} + \frac{\partial u_j}{\partial x_i} - \frac{2}{3} \delta_{ij} \frac{\partial u_l}{\partial x_l} \right) \right] \quad (7)$$

The mixture viscosity is determined using the kinetic theory of gases,

$$\mu = \sum_j \frac{X_i \mu_i}{\sum_j X_i \phi_{ij}} \quad (8)$$

where ϕ_{ij} and μ_i are given by

$$\phi_{ij} = \frac{\left[1 + \left(\frac{\mu_i}{\mu_j} \right)^{1/2} \left(\frac{M_{w,j}}{M_{w,i}} \right)^{1/4} \right]^2}{\left[8 \left(1 + \frac{M_{w,i}}{M_{w,j}} \right) \right]^{1/2}} \quad (8.1)$$

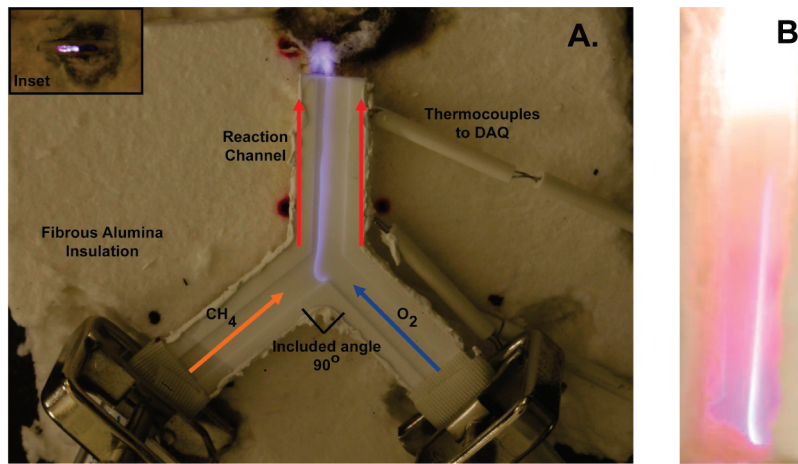


Figure 1. (A) Still-frame images depicting the layout of the microcombustor and the steady-state flame structure. The inset to part (A) shows the top view of the flame structure confined within the microcombustor, two flame cells and the edge-like flame are seen. (B) The edge-like flame only exists within the combustor, once the walls are sufficiently heated due to the presence of the external methane–air diffusion flame. A still-frame image of the flame cells is also shown in Figure 4. Total flow rate 300 sccm, with 100 sccm of CH₄.

and

$$\mu_i = 2.67 \times 10^{-6} \frac{\sqrt{M_{w,i} T}}{\sigma_i^2 \Omega_{\mu,i}} \quad (8.2)$$

The gas mixture thermal conductivity is determined from the thermal conductivity of each of the individual gases in the mixture using the ideal gas mixing law

$$\kappa = \sum_i \frac{X_i \mu_i}{\sum_j X_j \phi_{ij}} \quad (8.3)$$

The energy balance in eq 2 also accounts for the radiative heat transfer through the volumetric source term, S_h , as defined in the *Fluent* user manuals through the radiative transfer equation (RTE) and the weighted sum of gray gases model (WSGGM) model⁶⁰ is used to calculate the absorption coefficient. The RTE incorporated is

$$\frac{dI(\vec{r}, \vec{s})}{ds} + (a + \sigma_s)I(\vec{r}, \vec{s}) = an^2 \frac{\sigma T^4}{\pi} + \frac{\sigma_s}{4\pi} \int_0^{4\pi} I(\vec{r}, \vec{s}') \Phi(\vec{s} \cdot \vec{s}') d\Omega' \quad (9)$$

Of the radiation models available in *Fluent*, the P_N model has the broadest applicability for the work in this article. The equation used for solving the radiative flux was the P_1 model, which is the less complex case of the more general P_N models. The equations are developed by multiplying the RTE (eq 9) by various direction cosines to yield two moment equations, which can be integrated to yield the Milne–Eddington equations.⁶¹ The procedure is based on expansion of the local radiation intensity into an orthogonal series of spherical harmonics. The series is then truncated after a selected number of N terms.⁶¹ The model takes into account optical thicknesses in the range of optically thick (Roseland model) and thin mediums. The model also takes into account local emission and incoming and outgoing scattering from the gas mixture. The equation assumes the system to be in local thermodynamic equilibrium, which means that absorption in a small differential volume within the system is equal to the emission. For the CFD study reported, incoming and outgoing scattering was not considered and, as a consequence, anisotropic scattering can be neglected. The absorption coefficient of each species could be evaluated by calculating the WSGGM.⁶⁰ This method is implemented by fitting the absorption coefficient (eq. 9) and the emissivity factor in eq

(10) known to tabulated experimental values. The P_N model is used to determine the emissivity

$$\varepsilon = \sum_{i=0}^I a_{e,i}(T)[1 - e^{-k_i P S}] \quad (10)$$

and radiation flux is related to the incident radiation by

$$q_r = -\frac{1}{3(a + \sigma_s) - C\sigma_s} \nabla G \quad (11)$$

However, radiation intensity is also needed, which is related to the radiation flux by

$$q_r = \int_{\Omega'} I(r, \Omega') l d\Omega' \quad (11.1)$$

as described previously for radiating gas flow.⁶² To obtain the temperature, radiative intensity, and the radiation flux, the RTE, the energy equation, and eq 11 need to be solved simultaneously.^{59,61,63} The governing equations, mesh size, time-step, activation energy for flame ignition, and modeling methodology is similar to the CFD approach reported recently by some other researchers,^{44,64,65} suggesting that the approach used for developing a model to validate experimental observations is based on acceptable methods already published.

Results and Discussion

One of the ways to better understand the microcombustion process is to observe and characterize the parameters that affect flame structure. The observed steady-state flame structure and subsequent heat output of the microcombustor, which is important for many applications, is strongly affected by

(60) Smith, Z. F.; Shen, F. Evaluation of coefficients for the weighted sum of gray gases model. *Journal of Heat Transfer* **1983**, *104* (4), 602–608.

(61) Siegel, R.; Howell, J. R., *Thermal Radiation Heat Transfer*, 2nd ed.; Hemisphere Publishing Corporation: WA, 1981.

(62) Cheng, P. Two-dimensional radiating gas flow by a moment method. *AIAA J.* **1964**, *2* (9), 1662–1664.

(63) Incropera, F. P.; DeWitt, D. P., *Fundamentals of Heat and Mass Transfer*, 4th ed.; John Wiley and Sons: New York, 1996.

(64) Deshmukh, S. R.; Vlachos, D. G. CFD simulations of coupled, countercurrent combustor/reformer microdevices for hydrogen production. *Ind. Eng. Chem. Res.* **2005**, *44*, 4982–4992.

(65) Sarli, V. D.; Marra, F. S.; Benedetto, A. D. Spontaneous oscillations in lean premixed combustors: CFD simulation. *Combust. Sci. Technol.* **2007**, *179*, 2335–2359.

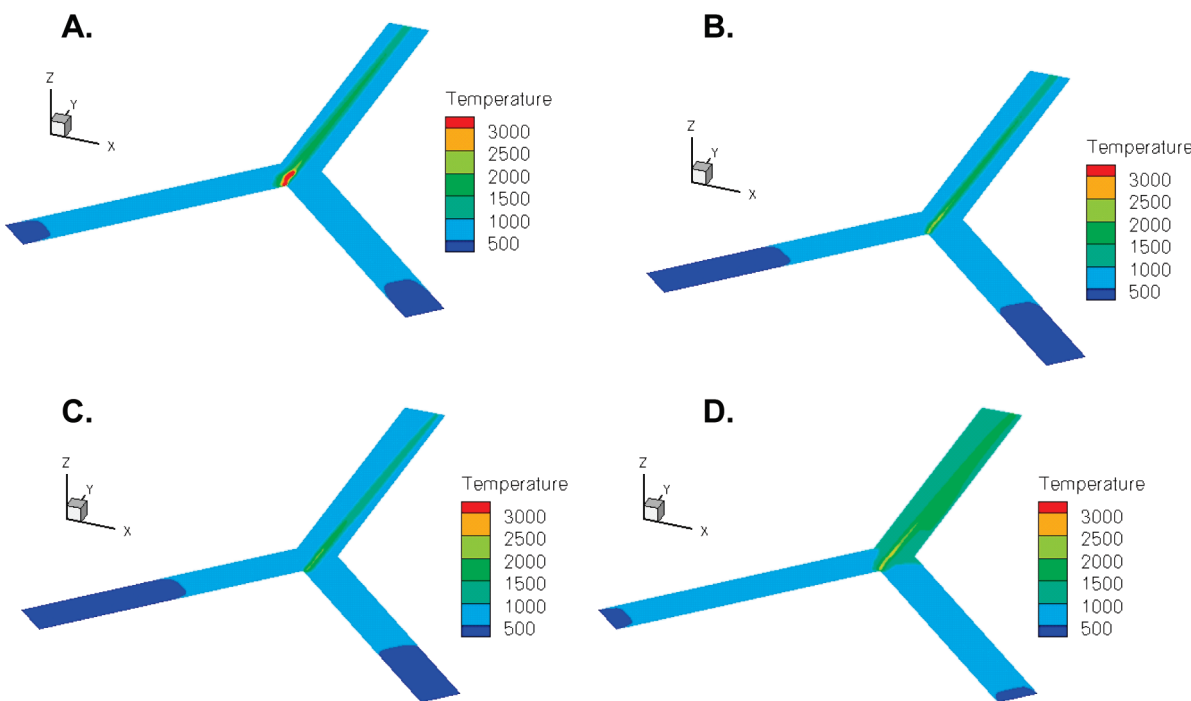


Figure 2. CFD model results for the central plane temperature in the fluid within the microcombustor for varying relative inlet flow rates. Total flow rate for all cases is 300 sccm. (A) 100 sccm of CH₄ and 200 sccm of O₂, (B) equal CH₄ and O₂ flow rates, (C) 200 sccm of CH₄ and 100 sccm of O₂, and (D) equal CH₄ and O₂ flow rates but the external walls except at the gas inlets and outlets are modeled as adiabatic. The boundary conditions at the inlet and outlet are the same as those in cases (A)–(C). In cases (A)–(C), the combustor loses heat to the environment by convection (natural convection coefficient assumed to be 10 W/m²·K) and by radiation to the surroundings at 300 K.

various environments in which the microcombustor is operated, leading to different boundary conditions for the model. This article serves to elucidate the influence of inlet flow conditions and thermal boundary conditions on the steady-state flame structure.

Figure 1 shows still-frame images for the layout of the microcombustor and the flame structure. The steady-state flame structure comprises discrete burning zones. The flame structure consists of an anchored edge-like flame at the inlet to the combustor channel and discrete flame cells. The number, relative location, and the shape of the flame cells have been the subject of other studies.^{23,30} Part B of Figure 1 shows that at elevated temperatures (>600 °C) no flame cells are observed and the anchored edge-like flame at the inlet extends through approximately 75% of the combustor channel length. Next, the results from the CFD model are presented to explain some of the experimental observations presented in Figure 1.

Figure 2 shows the CFD model results depicting the temperature of the fluid in the central plane within the microcombustor. It should be noted that the fluid temperature of the central plane correlates to the flame temperature, but for cases where the relative inlet flow rates of methane and oxygen are not equal, the flame is not confined to the middle of the combustion channel with respect to the lateral (*x*) direction. Furthermore, diffusive mixing between the fuel and oxidizer can also cause deviations from the center line in the axial direction, as discussed later. The deviation of the flame from the center of the channel has also been verified experimentally as seen in part B of Figure 1 (also Figure 4). Parts A–C of Figure 2 present CFD results for various inlet fuel oxidizer ratios. The boundary conditions for these cases allow for heat loss to the surroundings by natural convection and radiation. It can be seen from parts A–C of Figure 2 that with increasing CH₄ inlet flow rate the flame appears to bend toward the O₂ side. In addition, the highest gas-phase temperature occurs at the inlet in part A of Figure 2 with local fuel–oxidizer ratios similar to the stoichiometric

conditions for a premixed methane–oxygen flame. It can also be observed from part B of Figure 2 that the flame (case of equal flow rates) also deviates from the central plane, especially near the exit. Part D of Figure 2 corresponds to the case where the relative inlet flow rates are equal (same flow conditions as part B of Figure 2) but the lateral walls of the microcombustor are considered to be adiabatic. The gas inlets and the combustor exit are now heat sinks and the flame is observed to deviate or bend further toward the oxygen side as compared to part B of Figure 2. Figure 2 also shows that the temperature within the fluid is well below the adiabatic flame temperature (~3054 K) for methane–oxygen systems except near the inlet for the condition with 100 sccm of CH₄ and 200 sccm of O₂, which would be similar to the stoichiometric condition for a premixed case at the inlet to the microcombustor. One further observation for part D of Figure 2 is that once the lateral walls are insulated the temperature within the fluid rises and also spreads in the lateral direction. This is an important observation as it can help provide further direction for designing and building microcombustion systems with controllable and uniform heat output, which in the past has been a challenge.^{3,66}

Figure 3 presents some more CFD results depicting the temperature contours for the outside wall temperatures for the conditions discussed in Figure 2. It can be noted from Figure 3 that the wall temperatures are significantly lower than the temperature of the confined fluid. Also, large temperature gradients exist (can be over 100 °C/cm) on the external combustor walls, confirming previously reported experimental results.^{30,67} It can be seen from Figure 3 that the gas inlet legs (where no flame exists) in the Y-shaped microcombustor also

(66) Vican, J.; Gajdeczko, B. F.; Dryer, F. L.; Milius, D. L.; Aksay, I. A.; Yetter, R. A. Development of a microreactor as a thermal source for microelectromechanical systems power generation. *Proceedings of the Combustion Institute* **2002**, 29, 909–916.

(67) Miesse, C. M. Development of microcombustors and characterization of confined sub-millimeter laminar diffusion flames, Ph.D. Thesis, University of Illinois, Urbana, 2005.

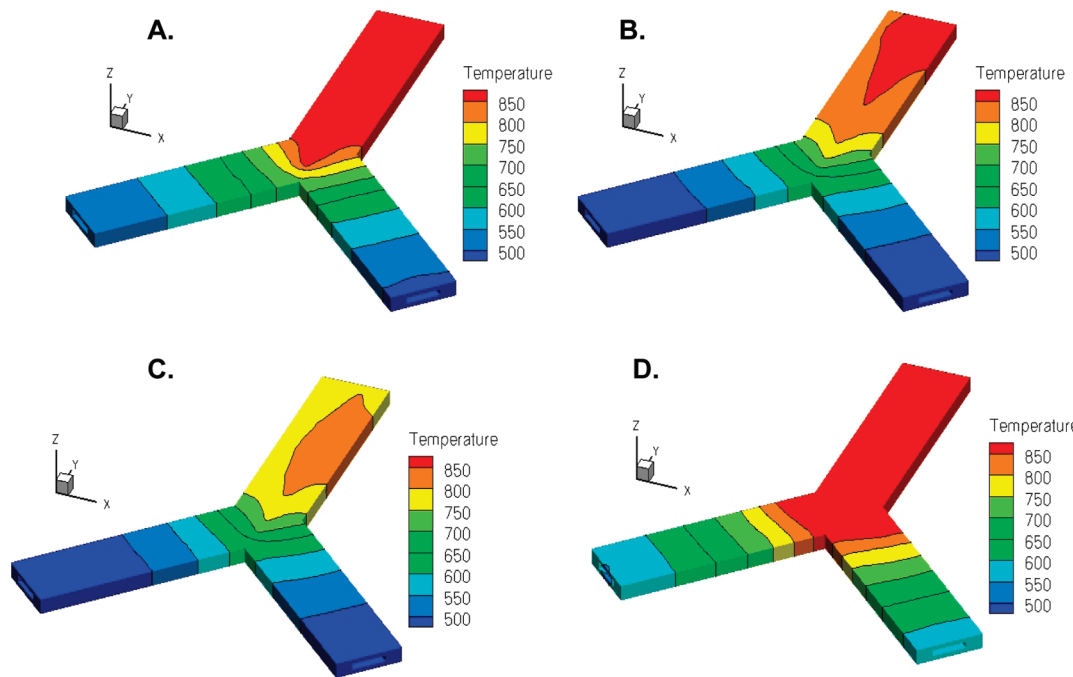


Figure 3. CFD model results showing the temperature contours for the external walls of the microcombustor for varying relative inlet flow rates. Total flow rate for all cases is 300 sccm. (A) Equal CH₄ and O₂ flow rates, (B) 100 sccm of CH₄ and 200 sccm of O₂, (C) 200 sccm of CH₄ and 100 sccm of O₂, and (D) equal CH₄ and O₂ flow rates but the external walls except at the gas inlets and outlets are modeled as adiabatic. The boundary conditions at the inlet and outlet are the same as in cases (A)–(C). In cases (A)–(C), the combustor loses heat to the environment by convection (natural convection coefficient assumed to be 10 W/m·K) and by radiation to the surroundings at 300 K.

have a significant temperature (500 °C or greater). Therefore, as the combustion process proceeds and heat generation occurs, the incoming gases undergo preheating. Experimentally, the heating of the gas inlet combustor legs was a problem in establishing secure gas inlet connections, which would often melt and cause gas leaks. However, the problem was resolved by using high-temperature ceramic tape to secure the connections. The preheating of incoming gases can be important as heat loss in microcombustion is often an area of concern.³ Part D of Figure 3 shows that the temperature distribution on the outside combustor wall is more uniform if the lateral walls are adiabatic. Once again, this result points to the value of thermal management in microscale combustion systems, which has been the subject of significant debate in the research community.^{3,68} Furthermore, in terms of developing design rules for building microcombustors the uniformity of external wall temperatures can be a significant consideration. It should be noted that, for the temperature predictions reported here, the radiation models are extremely important. In all models when radiation was ignored, the results generated by *Fluent* were not physically realistic and also did not match experimental observations at all. Therefore, as design rules for microcombustors are developed, heat loss through radiation will also be an important consideration. It can be seen from part A of Figure 2 and part A of Figure 3 that for the local fuel-oxidizer conditions, which are stoichiometric at the inlet, the fluid temperature and the wall temperature are higher than the other cases. In fact, near the anchor point, the CFD model predicts temperatures close to the adiabatic flame temperature (~3000 K for CH₄–O₂ mixtures) in the gas phase as seen in part A of Figure 2. These results also correlate to the experimental observations (part B of Figure 1) where it was noticed that the local stoichiometric case at the inlet produces higher recorded wall temperatures than other inlet

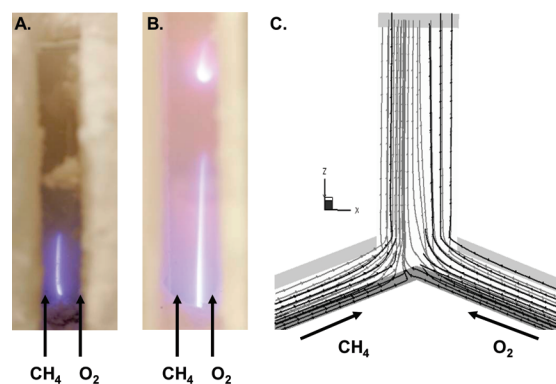


Figure 4. Figure shows the effect of mixing near the inlet to the combustion channel as the fuel and oxidizer come together. Even for equal flow rates of fuel and oxidizer, a small deviation from the center line is observed at the inlet. This is predicted by the streamlines in (C). Also, notice the bend in the flame structure toward the oxygen side in (B). Similar flame bending is observed in the CFD models also (parts (A) and (D) of Figure 2). A highly pronounced bend at the inlet occurs for asymmetric flow rates (part (A) of Figure 1).

flow conditions. One more point to note about the CFD results presented in Figure 3 is that the highest wall temperature exists at the exit to the combustor similar to the experimental observations where the highest external wall temperature was recorded near the exit to the microcombustor. In addition, the general trends for temperature predicted here are in agreement with normal scale combustion⁶⁹ and previously reported experimental data for microcombustors.³⁰

The shape of the steady-state flame structure was also investigated as a function of relative inlet flow rates with parts A and B of Figure 4 showing still-frame images for two possible steady-state configurations of the flame structure. It was

(68) Chandrasekharan, R.; Prakash, S.; Shannon, M. A.; Masel, R. I. Change in radiative optical properties of Ta₂O₅ thin films due to high temperature heat treatment. *Journal of Heat Transfer* 2007, 129, 27–36.

(69) Kuo, K. K. *Principles of Combustion*. John Wiley & Sons: New York, 1986.

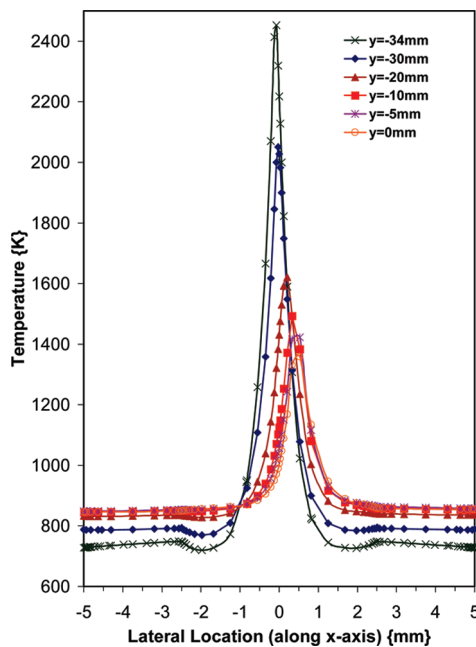


Figure 5. Parametric plot of the temperature as a function of the lateral direction (x) at various locations along the flow or y direction. The highest temperature occurs at the inlet to the combustion chamber, where the fuel and oxidizer initially meet and combust. The temperature distribution is symmetric with respect to the x axis.

observed (Figure 1 and Figure 4) experimentally that the flame deviates from the center line location if the fuel or oxidizer have a higher relative flow rate. This deviation is understandable as a higher volumetric flow rate implies a higher mass and volume occupied by gas with the higher inlet flow rate. To minimize volumetric changes and flow shearing effect, several experiments were conducted at equal volumetric flow rates (150 sccm each) and hence equal flow velocity (~ 0.67 m/s) of fuel and oxidizer. However, it was observed that even with equal flow rates a small deviation from the center line occurs and is also predicted by the streamlines in the CFD model. The edge-like flame anchored at the inlet is also observed to bend toward the oxygen side as the temperature increases (part B of Figure 4), and is also predicted by the *Fluent* calculations (parts B and C of Figure 2). This flame bending can be understood based on the local fuel–oxidizer ratios. In each of the cases where flame bending is observed, the combustor is being run under fuel-rich conditions at the inlet. To sustain to the gas-phase reactions, the flame bends toward the oxygen side. Furthermore, the diffusion coefficient of methane is higher than that for oxygen, which shifts the reaction toward the oxygen side of the flow. Manipulating the relative inlet mixture composition, in principle, can provide another operational control parameter for the design and operation of microcombustors.

Figure 5 depicts the temperature at various y locations as a function of the lateral direction (x). The inlet to the combustion chamber is at $y = -34$ mm and the exit to the combustion chamber is at $y = 0$ mm. Following the temperature contour plots for the confined fluid in Figure 2 and the parametric plot in Figure 5, it can be observed that the highest temperature occurs at the inlet to the combustion chamber within the fluid. It can also be observed that the temperature distribution is symmetric with respect to the x axis. However, as the flow moves further downstream (toward $y = 0$) the temperature distribution is observed to be no longer symmetric about the center line ($x = 0$) with the temperature being higher on the oxygen side. The higher temperature on the O_2 side can be understood based on the relative mixing of the fuel and oxidizer

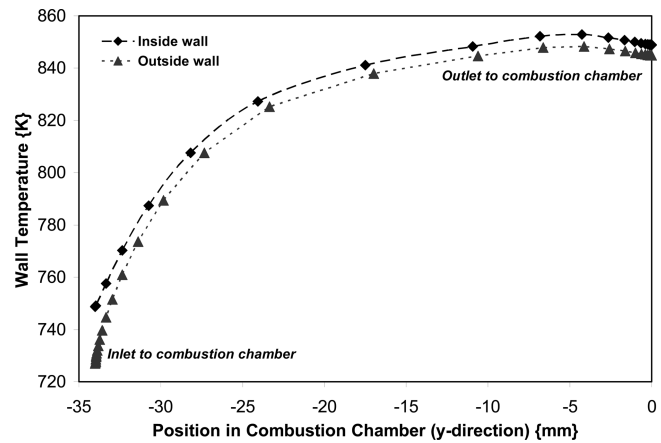


Figure 6. Wall temperatures rise steadily in the axial direction due to the continuous heat generation resulting from the combustion. It is to be noted that the gradient is quite steep at the inlet of the combustion chamber and gradually decreases in the axial direction as the rate of combustion is reduced.

and the reactions within the flow occurring off the center line, as discussed above. Figure 6 presents line plots for the contour plots of the microcombustor walls described in Figure 3. It can be observed that, for the representative lines plotted in Figure 6 for the center of the channel in the z direction ($z = 1$ mm) on the methane side of the combustion chamber, the wall temperatures rise steadily in the y direction as flow goes from the inlet to the outlet of the microcombustor due to the continuous heat generation resulting from the combustion process. The gradient between the inside wall, in contact with the reacting flow, and the outside wall is on the order of about ~ 20 K. Furthermore, it is to be noted that the gradient at the inlet of the combustion chamber reaches an almost 50 K change within a distance of less than 1 mm in the direction of bulk flow. This temperature gradient decreases by 10 times near the exit (~ 10 K over the last 2 mm) as the flow moves from the inlet toward the exhaust with the external diffusion flame extinguished. One caveat with respect to the CFD temperature gradient data discussed above is that the model fails to capture the discontinuous flame structure and instead predicts a continuous flame confined within the microcombustor. The formation of the discontinuous flame structure and presence of flame cells continues to remain an open question, despite several discussions in literature related to instabilities in non-premixed flames.^{27,30,40,45,53,70} In addition, the effect of surface reactions has also been neglected in the present study. As a consequence, the CFD model predicts temperature gradients that are lower than the experimentally observed temperature gradients. The under-prediction of temperature gradients is due to the fact that there are no localized zones with high or low temperature that would arise due to a discontinuous flame structure, which implies that for the CFD model a relatively uniform temperature distribution exists and hence the predicted temperature gradients are lower than those measured experimentally.

Thermal boundary conditions were also investigated to determine their importance on the confined flames. The thermal conductivity of the external combustor wall was altered by attaching a metal plate (Mo coated with Pt, to prevent oxidation of the Mo). It was expected that the metal plate would assist in spreading the heat more uniformly along the length of the

(70) Prakash, S.; Armijo, A. D.; Masel, R. I.; Shannon, M. A. In *Unsteady flames in microcombustion*, ASME International Mechanical Engineering Congress and Exposition, Chicago, IL, November 5–10, 2006; Chicago, IL, 2006.

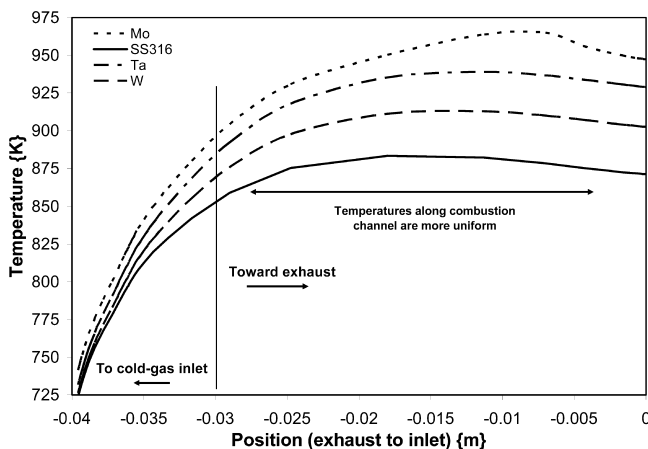


Figure 7. Predicted temperature profiles along the external wall for the heated exit boundary condition. The combustor channel is modeled as 40 mm length. Equal flow rates of CH_4 and O_2 are considered with a total flow rate of 300 sccm. The majority portion of the combustor channel is noted to have a uniform temperature distribution. The data presented is for a parametric study of various wall materials.

Table 1. Thermal Properties of Wall Materials

material	thermal conductivity (W/m·K)	emissivity
alumina	24	0.45
stainless steel 316	21.5	0.4
tantalum	57.5	0.2
molybdenum	138	0.2
tungsten	173	0.3

combustor channel. Indeed, the thermal energy was spread more uniformly and the temperature distribution with large gradients ($>100\ ^\circ\text{C}/\text{cm}$) along the length of the combustor become negligible ($\sim 10\ ^\circ\text{C}/\text{cm}$ or less).⁵¹ To validate the experimental data and better understand the role of attaching an external metal plate to the combustor wall, a CFD parametric study was conducted by varying the type of metal plate used. Four different metals that can sustain high temperatures were chosen: molybdenum (Mo), stainless steel 316 (SS 316), tantalum (Ta), and tungsten (W). Stainless steel has the lowest thermal conductivity, $k = 21.5\ \text{W}/(\text{m}\cdot\text{K})$ (emissivity 0.4) and tungsten the highest thermal conductivity, $k = 173\ \text{W}/(\text{m}\cdot\text{K})$ (emissivity 0.3) among the four materials chosen (Figure 7). Ta and Mo lie in between with respect to the thermal conductivity. The material properties used in the model are tabulated in Table 1. It can be seen from Figure 7 that the material with the highest emissivity (stainless steel 316, Table 1) leads to the highest heat loss due to radiation from the wall to the surroundings at room temperature and hence causes the external combustor walls to be the coolest by comparison. The stainless steel–alumina composite wall has a maximum temperature $\sim 880\ \text{K}$, whereas the walls with lowest emissivity metals attached (Ta, Mo) reached a maximum temperature on the order of 950 K. It should also be noted that the CFD code predicts that by attaching metallic layers to the outside wall the temperature gradients along the wall can be reduced to about $50\ ^\circ\text{C}/\text{cm}$ from $>100\ ^\circ\text{C}/\text{cm}$ in agreement with the assertion that metal plates on the outside walls assist in spreading the heat more uniformly along the combustor wall. However, it must be once again pointed out here that whereas the CFD model validates the global trend in experimental data for lower temperature gradients along the external wall, the model underpredicts the actual temperature gradient in contrast to the experimental data. This underprediction is attributed to the differences in the experimentally observed and model-predicted flame structures, as discussed above.

The last boundary condition evaluated was the effect of a heat source at the exit as heat loss in microcombustion often is considered a major hurdle toward developing systems with reproducible heat output.^{3,30,35–37,51} Toward the goal of evaluating the effect of an external heat source, the boundary condition at the outlet is changed so that the temperature of air at the combustor exit is 3000 K; close to the adiabatic flame temperature of methane–oxygen combustion. Experimentally, this case can be considered as the presence of an external diffusion flame at the exit (part A of Figure 1). One caveat with respect to the model conditions must be presented here. The boundary condition modeled is for thermal effects only: the species transport and interactions between an external flame and the confined flame are neglected in the CFD model. The CFD model predicts that the temperature of fluid in the central plane can increase to greater than 2500 K and the external wall temperature also reaches a maximum value of close to 1500 K. The high temperatures can be visually verified from part B of Figure 1, as observed from the glowing alumina walls (minimum temperature for alumina to visibly glow $\sim 600\ ^\circ\text{C}$). In previous studies, wall temperatures of approximately 1200 °C have been reported.²³

Conclusions

The modeling results validate the global temperature trends for measured external wall temperatures; however, the CFD model fails to capture the intricate details of the flame structure. For example, experimental data shows that by attaching a metal plate to the outside wall temperature gradients along the wall can be reduced. The same is observed in the CFD model reported here where temperature gradients along the wall reduce from $>100\ ^\circ\text{C}/\text{cm}$ to on the order of $50\ ^\circ\text{C}/\text{cm}$. In addition, inclusion of radiative heat transfer is important toward accurate modeling of thermal conditions for the microcombustor as it has been shown in this article that ignoring radiation leads to unphysical results with predicted flame and wall temperatures deviating significantly from experimental results. The inlet flow conditions influence the shape and location of the flame within the microcombustor. This article shows that by carefully engineering the various boundary conditions such as the wall thermal conductivity, wall emissivity, and inlet flow conditions, the external wall temperatures and flame structure can be manipulated for possibly developing more efficient microcombustion systems with controllable, repeatable, and uniform heat output. It is hoped that this work will provide a platform for developing design rules toward better engineered microcombustors for varied applications in small-scale and portable power systems.

Acknowledgment. This work was supported by the Department of Defense Multidisciplinary University Research Initiative (MURI) program administered by the Army Research Office under grant DAAD19-01-1-0582. The authors thank Prof. Richard Masel and Dr. Craig Miesse for assistance during various phases of this work. The authors thank the Rutgers University Academic Excellence Fund (AEF) for financial support.

Nomenclature

Symbol, Description

Y , local mass fraction of species.

ρ , mixture density.

\bar{v} , mixture velocity field.

\bar{J} , diffusive flux of species.

R , net rate of production of a chemical species.

h , enthalpy of a chemical species.	\vec{s} , direction vector.
u , fluid velocity.	a , absorption coefficient.
κ , thermal conductivity of the mixture.	σ_s , scattering coefficient.
T , absolute temperature.	x_i , component of Cartesian coordinate system.
S_h , volumetric heat source defined by the user (e.g., radiation source term).	n , refractive index.
N , total number of gas-phase chemical species.	σ , Stefan–Boltzmann constant.
D_{ij} , binary mass diffusion coefficient.	\vec{s}' , path length vector.
∇Y , gradient of the mass fraction of species.	\vec{s}'' , scattering direction vector.
D_T , thermal diffusion coefficient.	Ω' , solid angle.
∇T , temperature gradient.	ε , emissivity.
M_w , molecular weight of species.	$a_{e,i}$, emissivity weighting factors for the i^{th} gray gas.
Ω_D , diffusion collision integral.	k_i , absorption, coefficient for the i^{th} gray gas.
p_{abs} , absolute pressure.	P , sum of partial pressures of absorbing gases.
σ_{ij} , the arithmetic mean of the diameters of molecules of species i and j .	S , path length.
X , mole fraction of species.	q_r , radiative flux.
p , mixture pressure field.	C , linear anisotropic phase function coefficient.
μ , dynamic viscosity of the mixture.	G , incident radiation.
δ_{ij} , Kronecker delta.	k , thermal conductivity of combustor wall (alumina or a composite with metal pieces).
Ω_w , Lennard–Jones parameter (<i>Fluent</i> database).	Subscript i , species i but if used in derivates with space coordinate, i denotes coordinate basis.
σ , Lennard–Jones parameter (<i>Fluent</i> database).	Subscript j or j' , species j or j' but if used in derivates with space coordinate, denotes coordinate basis.
\dot{R} , Arrhenius molar rate of creation/destruction of a chemical species.	
I , radiation intensity.	
\vec{r} , position vector.	EF900040Q